CHEMICAL PHYSICS

Direct observation of hyperpolarization breaking through the spin diffusion barrier

Quentin Stern[1]*, Samuel François Cousin[1], Frédéric Mentink-Vigier[2], Arthur César Pinon[3], Stuart James Elliott[4], Olivier Cala[1], Sami Jannin[1]

Dynamic nuclear polarization (DNP) is a widely used tool for overcoming the low intrinsic sensitivity of nuclear magnetic resonance spectroscopy and imaging. Its practical applicability is typically bounded, however, by the so-called "spin diffusion barrier," which relates to the poor efficiency of polarization transfer from highly polarized nuclei close to paramagnetic centers to bulk nuclei. A quantitative assessment of this barrier has been hindered so far by the lack of general methods for studying nuclear polarization flow in the vicinity of paramagnetic centers. Here, we fill this gap and introduce a general set of experiments based on microwave gating that are readily implemented. We demonstrate the versatility of our approach in experiments conducted between 1.2 and 4.2 K in static mode and at 100 K under magic angle spinning (MAS)—conditions typical for dissolution DNP and MAS-DNP—and directly observe the marked dependence of polarization flow on temperature.

INTRODUCTION

Hyperpolarization techniques are a broad set of methods for increasing the nuclear spin polarization substantially beyond the thermal equilibrium value, thereby providing a route to overcoming the low intrinsic sensitivity of nuclear magnetic resonance methods. Among the methods established over the past few decades, dynamic nuclear polarization (DNP) techniques have become a method of choice for a broad range of applications, from materials sciences (*1*) and biology (*2*) to preclinical research (*3*), to give a few outstanding examples. In a DNP experiment, the high polarization of unpaired electron spins is transferred to the surrounding nuclear spins by microwave irradiation. Typically, stable organic radicals serve as the source of electron spins, and DNP is performed in the solid state and at low temperatures, where the electron polarization is highest. The two most currently widespread variants of DNP are magic angle spinning DNP (MAS-DNP) (*4*) and dissolution DNP (*d*DNP) (*5*–*9*). The former is usually performed at temperatures around $T = 100$ K and magnetic fields of $B_0 = 9.4$ to 21.1 T (*10*), providing enhancements on the order of hundreds over thermal equilibrium. By contrast, *d*DNP is typically performed at around $T = 1.0$ to 1.6 K and $B_0 = 3.35$ to 10 T (*11*, *12*) and is followed by sample dissolution and transfer in the liquid state to a magnetic resonance imaging scanner (*3*) or nuclear magnetic resonance (NMR) spectrometer. Typical signal enhancements in *d*DNP experiments are on the order of tens of thousands over thermal equilibrium (*5*).

*d*DNP and MAS-DNP rely on four DNP mechanisms (*13*–*15*): the solid effect (SE), the cross effect (CE), the thermal mixing, and the Overhauser effect. In all cases, hyperfine interaction between electron and nuclear spins is required for polarization transfer. As the intensity of this interaction decays with the inverse cube of the distance between the spins (for the dipolar part), polarization transfer occurs with the highest probability at the shortest distance from the electron. Nuclei that are too distant from the electron for efficient direct interaction may polarize more rapidly indirectly by nuclear spin diffusion relayed DNP (*16*). However, the nuclear spins closest to the electron spin, called "core" nuclei, are effectively decoupled from the "bulk" spins. When the electron-nucleus interaction surpasses the internuclear interaction, nuclear flip-flops are not energy-conservative anymore, and therefore, spin diffusion in the vicinity of the electron spin is reduced, thus limiting the DNP performance. This concept, known as the spin diffusion barrier, was first proposed in the 1960s by Blumberg (*17*) to refine Bloembergen's model of relaxation by nuclear spin diffusion in paramagnetic crystals (*16*). Khutsishvili (*18*) proposed an alternative definition of the same concept and later applied it in the context of DNP (*19*). In the following years, the models of Khutsishvili and Blumberg were extended by others to more experimental cases (*20*–*23*). Typical radii of the diffusion barrier were found to be on the order of 1 to 2 nm, depending on sample formulation and experimental conditions.

Early on, several authors found that spin diffusion was still possible among core spins, despite Blumberg and Khutsishlvili's predictions, either by theory (*24*–*27*) or experimentally (*28*). More recently, the introduction of *d*DNP and MAS-DNP has revived the interest in the question of the spin diffusion barrier (*29*–*42*). Most of these studies address the question of the diffusion barrier by comparing DNP build-up curves with models including DNP effects, diffusion, and relaxation. The existence of the diffusion barrier (or the slowdown of diffusion) is assessed indirectly based on the ability of the models to reproduce experimental DNP build-up curves. Two recent studies have approached the question experimentally using synthetic chemistry to precisely control the distance between the electron and the closest nuclear spin (*35*, *37*). They were able to determine the minimal distance from the electron at which nuclei could contribute to the DNP enhancement of the bulk spins, for their respective samples and experimental conditions.

To the best of our knowledge, no experimental procedure has been reported as of yet that enables a quantitative assessment of the polarization flow in the vicinity of the electron. Here, we introduce a general and simple method giving access to such information in a wide range of experimental conditions. The key idea is to generate a large polarization gradient between the core and bulk spins using microwave gating (*43*) and to subsequently monitor the return of the bulk spins to thermal equilibrium. Typical results are presented in Fig. 1, which shows three experimental proton saturation recovery

[1]Univ Lyon, CNRS, ENS Lyon, UCBL, Université de Lyon, CRMN UMR 5280, 69100 Villeurbanne, France. [2]National High Magnetic Field Laboratory, Florida State University, 1800 E. Paul Dirac Dr, Tallahassee, FL 32310, USA. [3]Swedish NMR Center, University of Gothenburg, Gothenburg, Sweden. [4]Department of Chemistry, Crown Street, University of Liverpool, Liverpool L69 7ZD, UK.
*Corresponding author. Email: quentin.stern@protonmail.com

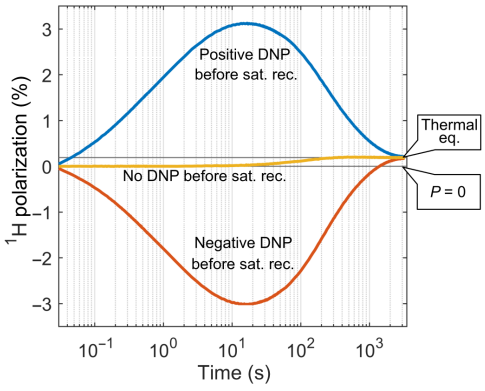

Fig. 1. Hyperpolarization resurgence. Saturation recovery recorded with small-angle pulses at 7.05 T and 3.8 K in static mode for sample I, after performing DNP in either positive or negative mode (i.e., yielding positive or negative nuclear polarization). Polarization surges far above and below from thermal equilibrium, respectively, before it finally relaxes toward it. The saturation recovery experiment recorded without prior microwave irradiation is shown for comparison.

curves for a sample of 1:3:6 H_2O:D_2O:glycerol-d_8 (v/v/v) (commonly known as "DNP juice") doped with 50 mM 4-hydroxy-2,2,6,6-tetramethylpiperidin-1-oxyl (TEMPOL) radical (sample I) at 3.8 K and 7.05 T. We recorded saturation recovery after performing DNP in either positive or negative mode (that is, setting the microwave frequency so as to yield positive or negative nuclear polarization, respectively) and without prior microwave irradiation. Saturation recovery experiments start with a train of saturation radio-frequency (rf) pulses, which should "erase" the memory of the system. Yet, because the pulses have a limited bandwidth, they do not affect the core spins whose resonance is strongly shifted by the nearby electron. During the saturation recovery recorded with prior microwave irradiation, polarization spreads from core to bulk spins, causing strong overshoots, which substantially exceed the intensity of thermal equilibrium toward, which all three curves tend. The sign of the overshoot reflects the sign of the DNP that was built before recording the saturation recovery. This experiment gives direct access to the dynamics of the polarization flow from core to bulk spins as their equilibration is time-resolved.

We dub our method HypRes (for *hyp*erpolarization *res*urgence). In the following, we show the applicability of HypRes on sample I at 1.2 to 4.2 K and 7.05 T in static mode. We develop a simple model that treats the spin system as two reservoirs, visible and hidden, connected by a flow rate. We find that between 1.2 and 4.2 K, the flow rate spans over two orders of magnitude and is faster than relaxation toward thermal equilibrium. A second variant of the HypRes experiment, including the manipulation of the spins nearest to the electron with broadband adiabatic pulses, probes indirectly spin diffusion occurring among the hidden spins. We show that spins closer than 0.3 nm to the electron can still exchange polarization with the bulk spins, in line with the recent literature (*35*, *37*). These measurements also provide experimental evidence for the theoretical prediction that with decreasing distance between nuclear and electron spins, the polarization exchange by spin diffusion slows down. Last, we show that the method is also compatible with MAS-DNP by applying it to a sample of 2:3 H_2O:glycerol (v/v) doped with 10 mM AsymPolPOK radical (*44*) (sample II) at 100 K and 14.1 T.

These new methods provide important insights into a very fundamental mechanism in DNP, namely, the flow of nuclear polarization away from paramagnetic agents to the bulk spins. While it was possible to study such processes indirectly using conventional saturation recovery experiments or DNP build-up curves, the HypRes approach offers the possibility of a more direct measurement in which the respective contributions of DNP and diffusion are disentangled. The model that we use here to extract quantitative information from the HypRes results is a first simplistic approach. However, these results could be used to test more profound models including mechanistic description of the polarization transfers among nuclei.

Theory and definitions

The definition of the spin diffusion barrier changes according to authors' choices and throughout the years of theoretical and experimental development. The size of the diffusion barrier may either be predicted by theory or determined experimentally. In essence, theoretical definitions are all based on the comparison of the interaction between nuclei and between an electron and nuclei. Blumberg's original definition sets the limit where the dipolar interaction between nuclei is equal to the interaction between the nucleus and the electron (*17*). Khutsishvili's definition sets the barrier where the difference in Larmor frequency of the nuclei caused by the electron is equal to the interaction between the nucleus and the electron, resulting in a shorter radius (*18*). These two definitions only take into account the secular term of the dipolar interaction between the electron and the nucleus. More recently, more sophisticated definitions of the diffusion barrier were proposed (*32*, *33*). Hovav *et al.*'s criterion includes the pseudo-secular contribution. Furthermore, it includes an arbitrary parameter ζ that determines to which extent diffusion is quenched within the barrier.

Figure 2A shows the dipolar coupling of a proton spin with an electron centered in a vertical plane, for both the exact form and taking its root mean square over all orientations. Figure 2B shows a visual representation of the diffusion barriers for sample I in red. The calculation of the barrier radius requires the determination of the distance between neighbor nuclei. Here, we have estimated the distance between neighbors assuming a statistical distribution of proton spins with the concentration of the solvent. Therefore, the resulting radii of the diffusion barriers are representative of diffusion among solvent protons and not among the protons of the radical itself, where the local density of proton spins is higher. The mathematical expressions and the details of how we calculated the different radii using these definitions are given in the Supplementary Materials. The radii of the diffusion barrier in Fig. 2B are compared with the mean volume per electron, represented in blue, which can be seen as the limits of the system. For all three definitions, the spin diffusion barrier is larger than the mean volume per electron. In other words, there should be no spin diffusion among the solvent protons of sample I. We ought to point out that these predictions are only rough estimates, which assumes that spins are statistically distributed in space.

In addition to theoretical definitions of the diffusion barrier, Wolfe (*28*) introduced an operational definition according to which spins are within the diffusion barrier if they are "in stronger contact with the lattice phonons that with the bulk spins," that is, if they relax faster than they can exchange polarization with the bulk spins. Wolfe determined experimentally that proton spins at 0.3 nm to the paramagnetic center were still in strong contact with the bulk spins and, hence, outside of the barrier, according to his definition (for proton spins separated by 0.16 nm in a paramagnetic crystal at 1.4 K and 1.6 T). This approach was used in other recent studies (*35*, *37*).

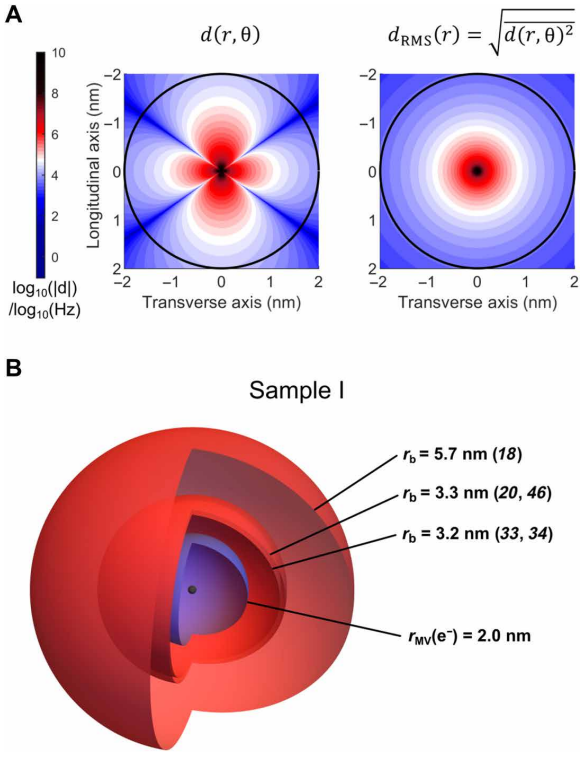

Fig. 2. Dipolar coupling and spin diffusion barrier. (**A**) Dipolar coupling of a proton and an electron spin taking the angular dependence into account $d(r,\theta)$ or as the root mean square $d_{RMS}(r)$, where r and θ are the distance between the electron and the nucleus and the angle between the vector connecting the electron and the nucleus and the main magnetic field, respectively. The black solid line represents the radius of the mean volume per electron in the case of sample I. The blue and red domains correspond to areas where proton spins are expected to contribute to the NMR line or not, respectively. (**B**) Representation of the spin diffusion barrier r_b for the solvent protons of sample I according to Blumberg (*17*), Khutsishvili (*19, 54*), and Hovav *et al.* (*32, 33*). (red spheres) compared with the mean volume per electron spin $r_{MV}(e^-)$ (blue sphere). The black sphere represents the electron.

It is common to call the spins that lie inside and outside of the spin diffusion barrier core and bulk spins, respectively. Assuming Wolfe's definition of the barrier, diffusion from core to bulk spins is impossible by the definition itself. Claims that diffusion is observed through the diffusion barrier only make sense with respect to theoretical definitions. The HypRes experiment monitors polarization flowing from spins that are inaccessible to NMR detection to those that are accessible. We will refer to them as hidden and visible spins, respectively, to avoid ambiguity. We note that the core spins—if any—are a subset of the hidden spins.

RESULTS AND DISCUSSION

HypRes experiment

The experimental procedure of the HypRes experiment is shown in Fig. 3. It consists of the following steps:

I) Full saturation. The polarization of the nuclear spins is wiped out so that the experiment starts in known conditions by a series of hard rf pulses (more details are available in the "Erasing the memory of the system between experiments" section in the Supplementary Materials).

II) Prepolarization. Microwaves are turned on during a delay set to be at least five times the proton DNP build-up time constant so that, when the microwaves are gated, the sample is assumed to have reached DNP equilibrium with a spatially homogeneous polarization P_{DNP}^{max}.

III) Visible spins saturation. The NMR signal is saturated using a train of hard rf pulses. Because the saturation pulses have a limited bandwidth, the spins that experience a strong dipolar shift due to a nearby paramagnetic center are not affected. The saturation scheme is optimized to be efficient for the visible nuclear spin with the polarization of the visible spins $P_v \sim 0$, while remaining as short as possible to leave the hidden nuclear spins unaffected with $P_h = (1 - \eta_{sat})P_{DNP}^{max}$, where η_{sat} is an attenuation factor ideally close to 0. The saturation block is terminated by a delay to accommodate acoustic ringing and allow the remaining transverse magnetization to dephase before detection. At this point, the proton spin system has polarization values $P_v \sim 0$ and $P_h = (1 - \eta_{sat})P_{DNP}^{max}$.

IV) Resurgence monitoring. The hyperpolarization resurgence is monitored for the visible spin reservoir by NMR acquisition blocks separated by time delays.

V) Decay monitoring. The return to thermal equilibrium is monitored.

Figure 4 shows a typical HypRes curve and its processing for sample I at 7.05 T and 3.8 K. More details regarding the experimental procedure and the processing of HypRes data are available in Materials and Methods and in the Supplementary Materials.

Two-reservoir model

A model is used to interpret the data assuming that the visible and hidden spins behave as reservoirs exchanging polarization at flow rate R_f and that each reservoir returns to thermal equilibrium with respective intrinsic relaxation rates, $R_{1,v}$ and $R_{1,h}$, which is reminiscent of typical spin temperature models (*14*). Figure 5 shows a schematic representation of the model. The underlying assumption is that diffusion within the reservoirs is fast with respect to the flow between them, which allows the polarization to be considered as "instantly" uniform inside each reservoir. This would be true if diffusion was not hindered by the presence of the electron. We estimate that diffusion connects the spins within a characteristic time of 100 ms or at a frequency of 10 s^{-1} in our conditions [this estimation is based on values from the literature (*45*); more details are available in the Supplementary Materials]. As will be revealed in Results, the measured flow rate is small compared to this characteristic diffusion rate. However, of course, diffusion is expected to be hindered by the presence of the electron. This simplification is a trade-off to describe the system with a simple model in first approximation. It is also assumed that no other reservoirs substantially influence the proton spin system. In particular, it is assumed, and later verified, that the deuterium nuclei present within the sample are not responsible for the observed effect.

Under the assumptions above, the evolution of the polarizations in the visible and hidden reservoir, $P_v(t)$ and $P_h(t)$, is given by the following differential equation

$$\frac{d}{dt}\begin{pmatrix} P_v \\ P_h \end{pmatrix} = \begin{pmatrix} -\chi_h R_f - R_{1,v} & \chi_h R_f \\ (1-\chi_h) R_{ex} & -(1-\chi_h) R_f - R_{1,h} \end{pmatrix} \begin{pmatrix} P_v \\ P_h \end{pmatrix} + P_{eq} \begin{pmatrix} R_{1,v} \\ R_{1,h} \end{pmatrix} \quad (1)$$

where χ_h is the fraction of the nuclear spins in the hidden reservoir and P_{eq} is the nuclear polarization at Boltzmann equilibrium. The

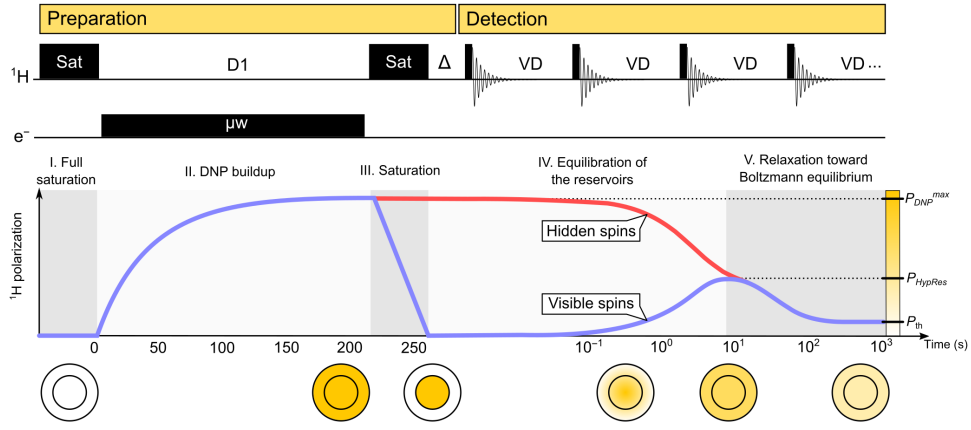

Fig. 3. HypRes experiment. Schematic representation of the HypRes experiment and its steps. During the preparation phase, polarization is built by microwave irradiation of the electron resonance (represented by the "μw" block). The polarization of the visible spins is then annihilated by a train of hard pulses (represented by the "Sat" block) during the detection phase. The polarization of the visible spins is monitored by small-angle pulses (represented by black rectangles) separated by variable delays (VD). The curves show the evolution of the visible and hidden spins during the course of the experiment. The circles below represent the polarization of the visible and hidden reservoirs (outer and inner circle, respectively), with darker shading indicating higher polarization.

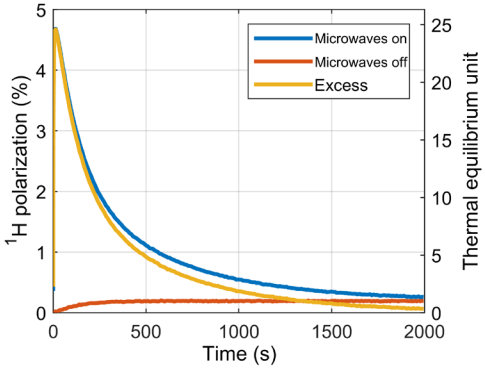

Fig. 4. Processing of HypRes results. The HypRes experiment is recorded with and without microwave irradiation, resulting in the microwave-on and -off curves, respectively. The microwave-off curve is subtracted to the microwave-on curve to yield a curve of polarization excess with respect to thermal equilibrium. Note that the microwave-off curve corresponds to a conventional saturation recovery experiment.

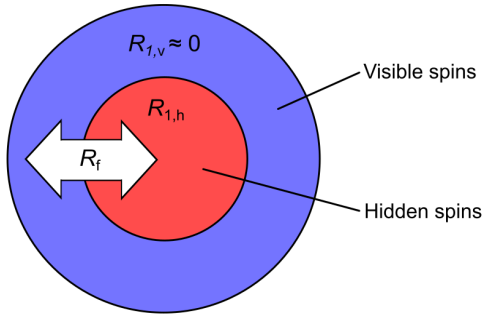

Fig. 5. Two-reservoir model. Schematic representation of the model used to analyze HypRes results. The relaxation rate constant of the visible spins $R_{1,v}$ is assumed to be negligible. Polarization flows between the visible and hidden reservoirs at flow rate R_f, while the hidden spins relax to thermal equilibrium at rate $R_{1,h}$.

derivation of the model is given in the Supplementary Materials. The solution to this differential equation is

$$\begin{pmatrix} P_v \\ P_h \end{pmatrix} = P_{eq} - \alpha V_- e^{\lambda_- t} - \beta V_+ e^{\lambda_+ t} \quad (2)$$

with the eigenvalues λ_+ and λ_- and eigenvectors V_+ and V_- given by

$$\lambda_\pm = \frac{-R_f - R_{1,v} - R_{1,h} \pm \sqrt{(R_f + R_{1,h} - R_{1,v})^2 + 4\chi_h R_f (R_{1,v} - R_{1,h})}}{2}$$
$$V_\pm = \begin{pmatrix} 1 + \dfrac{R_{1,h} + \lambda_\pm}{R_f(1-\chi_h)} \\ 1 \end{pmatrix} \quad (3)$$

and the coefficients α and β, which depend on the initial conditions

$$\alpha = \frac{(\lambda_+ + R_{1,h})\left(P_{eq} - P_h^0\right) + (1-\chi_h) R_f \left(P_v^0 - P_h^0\right)}{\lambda_+ - \lambda_-}$$
$$\beta = \frac{(\lambda_- + R_{1,h})\left(P_{eq} - P_h^0\right) + (1-\chi_h) R_f \left(P_v^0 - P_h^0\right)}{\lambda_- - \lambda_+} \quad (4)$$

where P_v^0 and P_h^0 are the polarizations of the visible and hidden reservoirs at $t = 0$, respectively, which corresponds to the beginning of NMR signal detection. Because the visible reservoir is saturated, we have $P_v^0 = 0$. Because the polarization is assumed to be homogeneous throughout each reservoir at $t = 0$, the polarization of the hidden reservoir is equal to the polarization at the DNP equilibrium, that is, $P_h^0 = P_{DNP}^{max}$. The eigenvalues λ_+ and λ_- determine the two relevant time scales predicted by the model. $-\lambda_-$ corresponds to the rate at which the two reservoirs equilibrate with each other, while $-\lambda_+$ corresponds to the rate at which their polarizations return toward Boltzmann equilibrium, after equilibration. This rate thus corresponds to the longitudinal relaxation rate constant R_1, and so we write

$$R_1 = -\lambda_+ \quad (5)$$

In our conditions, we approximate that the intrinsic relaxation rate constant of the bulk spins $R_{1,v}$ is 0; that is, the visible spins only reach Boltzmann equilibrium through spin diffusion toward the hidden spins, which are efficiently relaxed by the nearby electrons (*17*, *19*). Because the curves obtained in the HypRes experiment are expressed in terms of polarization excess, the thermal buildup must be subtracted, yielding

$$\begin{pmatrix} PE_v \\ PE_h \end{pmatrix} = \begin{pmatrix} P_v \\ P_h \end{pmatrix} - P_{eq}(1 - e^{\lambda_+ t}) = -\alpha V_- e^{\lambda_- t} - (\beta V_+ - P_{eq}) e^{\lambda_+ t} \quad (6)$$

where PE_v and PE_h are the polarization excess in the visible and hidden reservoirs, respectively.

Experimental quantification the polarization flow as a function of temperature

The HypRes experiment was performed on sample I at 7.05 T in static mode between 1.2 and 4.2 K. The polarization excess along time is shown in Fig. 6A (gray crosses). During the preparation step, the sample was polarized in positive mode, causing a positive polarization overshoot. Because of the prohibitively slow relaxation at the lowest temperatures, the curves were not recorded until they had reached thermal equilibrium. In particular, at 1.2 K, the polarization had reached its maximum but was only starting to decay when the monitoring was stopped. The two-reservoir model described above was applied to these HypRes curves (black curves in Fig. 6A). As explained in the dedicated section, it was assumed that the polarization of the visible and hidden reservoirs at the beginning of detection was 0 and P_{DNP}^{max}, respectively, and that the intrinsic relaxation rate of the visible reservoir was negligible, $R_{1,v} \approx 0$. The three remaining free parameters are $R_{1,h}$, R_f, and χ_h. Their fitted values are shown in Fig. 6B. The flow rate R_f spreads over two orders of magnitude from 4.4×10^{-3} s^{-1} to 0.29 s^{-1}. The relaxation rate of the hidden reservoir R_h is not shown for 1.2 K because its fitted value is unrealistically small and out of the trend (the fitted value is between 10^{-14} and 10^{-11} s^{-1} depending on the starting point of the fit algorithm). However, neither the quality of the fit nor the fitted values of R_f and χ_h are significantly affected by the value of $R_{1,h}$ (the fit was repeated fixing $R_{1,h}$ between 0 and 10^{-5} s^{-1}, which did not affect R_f and χ_h significantly). For the available range, R_h spreads from 9.4×10^{-4} s^{-1} to 6.9×10^{-2} s^{-1}. The fitted size of the hidden reservoir χ_h is between 5 and 7%. We show in fig. S2 that the HypRes effect occurs also in a fully protonated sample, that is, in the absence of a deuterium spin reservoir.

The model fits the data appropriately during the decay of the curves, that is, once the strong polarization gradient between hidden and visible spins has already disappeared. As expected, the quality of fit is poorer at the beginning of the curve, during the equilibration. The simplicity of the model that assumes two homogeneous reservoirs does not account for the complex dynamics of the spin system, when gradients are equilibrating among the hidden spins. Nonetheless, it allows for at least an order of magnitude estimate of the flow between the reservoirs and shows its tremendous temperature dependence.

The relaxation rate of the hidden reservoir $R_{1,h}$ is found to be slow compared with the flow between the reservoirs R_f (the ratio $R_{1,h}/R_f$ goes from ~1/4 to ~1/27 at 4.2 and 1.8 K, respectively). This implies that the two domains of the HypRes curve (the equilibration and the decay) can be interpreted separately; the rise of the polarization excess informs on the flow between the reservoirs R_f, while the decay informs on the relaxation rate $R_{1,h}$. It also implies that polarization is able to equilibrate throughout the spin system before relaxation becomes substantial. In this limit, the size of the hidden reservoir is directly proportional to the intensity of the overshoot P_{HypRes}

$$\tilde{\chi}_h \approx \frac{P_{HypRes}}{P_h^0} = \frac{P_{HypRes}}{(1 - \eta_{sat}) P_{DNP}^{max}} \quad (7)$$

where η_{sat} and P_{DNP}^{max} are the attenuation of the polarization in the hidden reservoir caused by the saturation block at the end of preparation and the polarization measured at DNP equilibrium, respectively. The size of the hidden reservoir can be obtained with this method ($\tilde{\chi}_h$) or with the two-reservoir model (χ_h). While the latter is biased by the poor match of the two-reservoir model, the former gives a more direct estimate of the size of the hidden reservoir by the HypRes experiment. Figure 6B shows that the size of the hidden reservoir, evaluated with Eq. 7, seems to decrease when temperature increases. Two effects can explain this apparent dependence. First, because of the increase of flow rate R_f with temperature, more

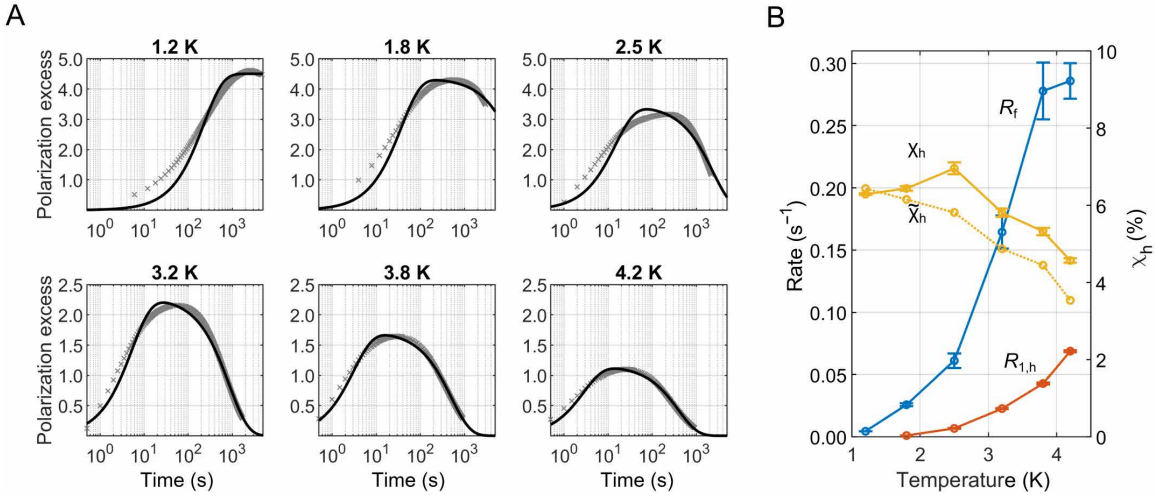

Fig. 6. Diffusion versus temperature. (**A**) Results of the HypRes experiment at 7.05 T in static mode between 1.2 and 4.2 K for sample I, monitored with small-angle pulses expressed in terms of polarization excess with respect to thermal equilibrium. The gray crosses and the black lines represent the experimental data and the fit of the two-reservoir model, respectively. (**B**) Fitted parameters of the two-reservoir model plotted against temperature. The size of the hidden reservoir is given according to the two-reservoir model (χ_h) and according to Eq. 7 ($\tilde{\chi}_h$). The error bars correspond to the error of the fit with 95% confidence.

polarization is able to leak out of the hidden reservoir during saturation at higher temperature. As the saturation scheme was identical for all six HypRes curves, an increased saturation of the hidden reservoir η_{sat} with temperature can be expected and thus a smaller "apparent" size. Second, the condition that the polarization flow is much faster than relaxation is better satisfied at the lowest experimental temperature.

The size of the hidden reservoir

The size of the hidden reservoir was quantified in a separate experiment for comparison with the values obtained above. The thermal equilibrium signal buildup of DNP juice was recorded as a function of TEMPOL concentration at 3.8 K and 7.05 T and fitted with a monoexponential model (see fig S3). Figure 7A shows how the thermal equilibrium signal decreases with increasing TEMPOL concentration. The signal was not recorded without TEMPOL because of the very slow relaxation of proton spins in the absence of paramagnetic relaxation. Assuming that the signal loss is linear with the TEMPOL concentration in the low range, we extrapolate the intensity at a concentration of 0 (here, we simply used the slope between the first two points) to normalize the curve with a *y* intercept of 100%. From this curve, we find that the presence of 50 mM TEMPOL in sample I removes ~30% of the proton signal.

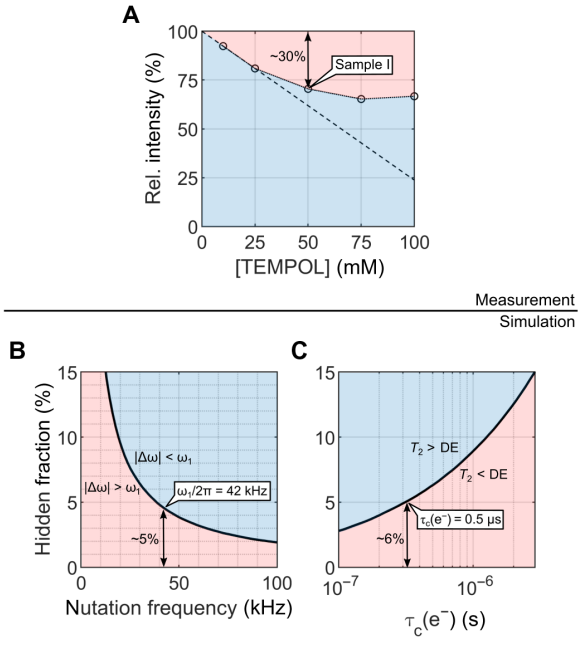

Fig. 7. Quantification of the hidden spins. (**A**) Relative proton signal as a function of TEMPOL radical concentration in DNP juice recorded at 7.05 T and 3.8 K in static mode (open circles) showing that the presence of the radical quenches ~30% of the NMR signal for sample I. The dashed line represents linear interpolation of the first two points. (**B**) Simulated fraction of the spins that are hidden because they are unaffected by rf pulses as a function of the pulse bandwidth. $\Delta\omega$ and ω_1 are the paramagnetic shift and nutation frequency of the pulses, respectively, used to discriminate between visible and hidden spins. (**C**) Simulated fraction of the spins that are hidden because their transverse relaxation time constant is below the dead time of the spectrometer as a function of the correlation time of the electron spin state. $T_{2,para}$ and τ_d are the transverse paramagnetic relaxation time constant and the spectrometer dead time, respectively, used to discriminate between visible and hidden spins. The light blue and pink areas represent the visible and hidden fraction of the proton spins, respectively. See the Supplementary Materials for details of the simulations.

Two effects may account for the signal loss in the presence of a paramagnetic species. First, the dipolar interaction with electrons shifts the Larmor frequency of the close nuclei outside the detection limits. Second, the interaction with electrons shortens the transverse relaxation time of the nuclei, an effect known as paramagnetic relaxation enhancement (PRE), which increases the signal loss during the dead time between the pulse and the acquisition (*46*, *47*). Figure 7 (B and C) shows simulations of the two contributions, which were performed assuming a random distribution of 1926 electrons in a cube of 40 nm (corresponding to the concentration of 50 mM). The proton paramagnetic shift was calculated taking into account the angular dependence of the dipolar interaction. Protons are considered undetectable when their paramagnetic shift is larger than the excitation bandwidth of the pulse, which we estimate to be equal to the nutation frequency (42 kHz). We find that ~5% of the spins are hidden according to this criterion [see Fig. 7B]. The transverse paramagnetic relaxation rate of the protons is calculated using the equation of PRE (*46*, *47*), which does not account for any angular dependence. Protons are considered to relax too rapidly to be detected when their transverse relaxation time constant is on the order of the dead time between the pulse and the signal acquisition (τ_d). Paramagnetic relaxation depends on the correlation time of the electron spin state $\tau_c(e^-)$, which we can only estimate to be on the order of 0.5 μs (see the Supplementary Materials). Figure 7C shows the fraction of spins that are hidden by PRE as a function of $\tau_c(e^-)$. We find that, for $\tau_c(e^-)$ = 0.5 μs, the hidden fraction is 6%. Details on the simulations are available in the Supplementary Materials. The contributions of the two effects simulated here may have different angular dependencies, but they do not add up together in such a way that could explain the experimentally determined signal loss of ~30% shown in Fig. 7A. This experimental result remains difficult to rationalize.

It should be noted that even if the PRE may contribute to the signal losses shown in Fig. 7A, it is not the effect that enables HypRes. In contrast, the frequency shift causes the protons near the electron spins to be immune to saturation pulses, which is the essential ingredient allowing the creation of a polarization gradient near the electron and, thus, for the HypRes effect. Our simulation shows that ~5% of the protons in sample I are beyond the bandwidth of the pulses, in reasonable agreement with the result of the HypRes experiment shown in Fig. 6 (hidden reservoir size between 5 and 7%). The HypRes experiment was repeated at 3.8 K and 7.05 T for sample I with various saturation pulse nutation frequencies (see fig. S5A). We found that the dependence of the hidden fraction on the nutation frequency of the saturation pulses follows the same trend for experiment and simulation (see fig. S5B).

HypRes using broadband inversion pulses

To gain further insight into the spin diffusion processes near the electron, we repeated the HypRes experiment at 3.8 K and 7.05 for sample I in static mode adding a broadband inversion pulse centered at the middle of the NMR line before saturating the visible spins (see pulse sequence in Fig. 8A). We used chirp pulses with widths of 0.5, 1, 2, 3, and 4 MHz, intended to invert proton spins over ±0.25, ±0.5, ±1, ±1.5, and ±2 MHz, respectively. These pulses thus invert proton spins far off resonance (from the detectable NMR range). After inversion, the spins are saturated by a train of pulses that act

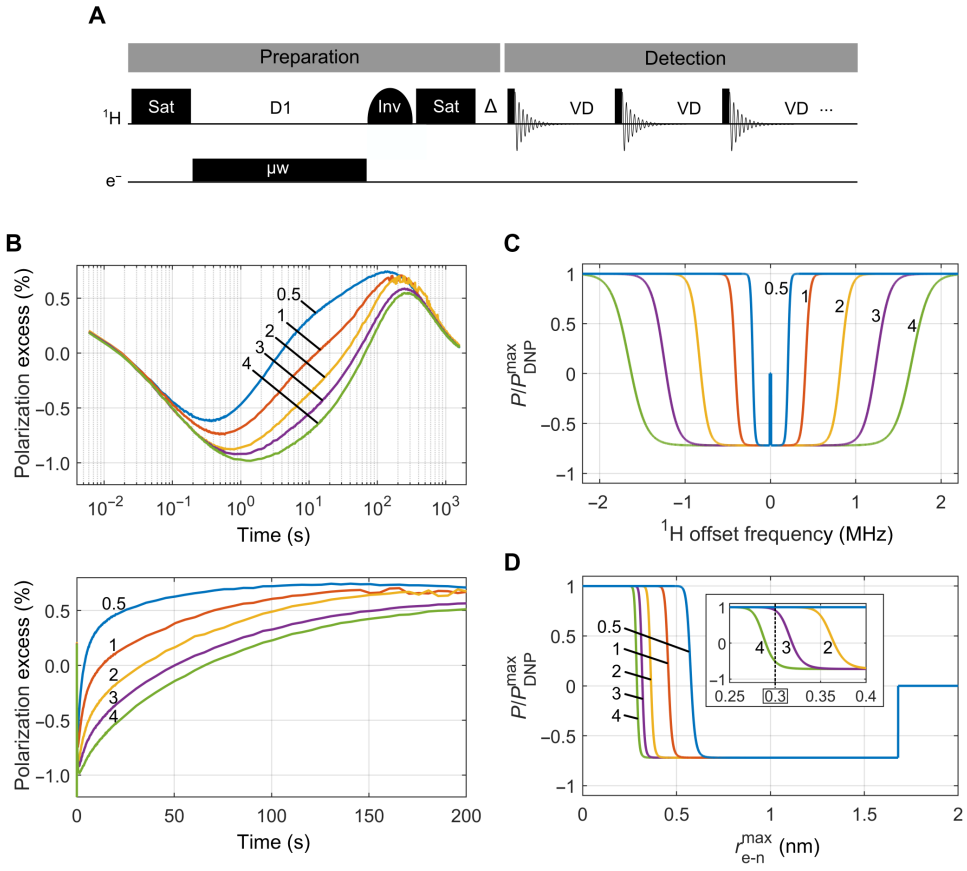

Fig. 8. HypRes experiment with inversion pulses. (**A**) Pulse sequence of the HypRes experiment including a broadband adiabatic pulse at the end of the preparation step (represented by the shape labeled "Inv"). (**B**) Results of the HypRes experiment with inversion pulses at 7.05 T and 3.8 K in static mode recorded with small-angle pulses for sample I with inversion widths from 0.5 to 4 MHz, in logarithmic and linear scale. (**C**) Estimated relative polarization profiles of the proton spins at the end of the preparation as a function of Larmor frequency shift taking into account the imperfection of the pulses (see the Supplementary Materials for more information on the pulse imperfections). The dip near zero is due to the narrow band saturation at the end of the preparation phase. (**D**) Estimated relative polarization profiles of the proton spins at the end of the preparation as a function of the distance to the electron spin, converted from (C) using Eq. 8. The numbers by the curves in (B) to (D) indicate the theoretical widths of inversion chirp pulses in megahertz.

only on a narrow bandwidth (see above), as in the pulse sequence presented in Fig. 3.

At the end of the preparation, the proton spins can be separated into three parts:

1) Those far from the electron have a polarization of 0 due to the narrow saturation pulses.

2) Those closer to the electron that have been inverted by the broadband pulse have polarization with opposite sign compared to what they acquired under DNP (but reduced by the inversion pulse imperfection).

3) Last, those that are close enough to the electron with Larmor frequencies outside of the range of inversion of the pulse have kept the sign of polarization that they acquired under DNP.

Following preparation, the signal resurgence is recorded by small-angle pulses, varying the delay between the detection blocks to capture processes occurring on all time scales. Figure 8B shows the resulting HypRes curves. On a fast time scale of hundreds of milliseconds to seconds (depending on the inversion width), the inverted hidden spins equilibrate their polarization with the visible spins, causing a negative overshoot. Then, on a longer time scale of hundreds of seconds, the polarization of the spins that had not been inverted and had, therefore, kept their positive polarization reaches the visible spins causing a positive polarization overshoot.

The width of the inversion pulses influences the curves in several regards. First, the wider the inversion, the stronger the negative overshoot and the weaker the positive overshoot, which is consistent with the assumption that more spins are inverted with a larger pulse bandwidth and that they do exchange polarization with the visible spins. Second, the wider the range of inversion, the later the negative extremum is reached (after 0.4 and 1.4 s for the 0.5- and 4-MHz inversion pulses, respectively), and the same is true for the positive extremum (after 150 and 300 s for the 0.5- and 4-MHz inversion pulses, respectively). A larger pulse inversion bandwidth implies that the noninverted spins are more coupled to the electron. Therefore, the fact that the overshoot occurs later demonstrates that the stronger the protons are coupled with the electron, the more spin diffusion is hindered. Last, the slopes of the curves going from the negative to the positive extrema are also affected by the inversion width that supports this argument. These measurements thus provide experimental evidence that the Larmor frequency gradient caused by the electron spin is responsible for a gradient of the nuclear spin diffusion coefficient. We note that the shift of the nuclear

Larmor frequency caused by the hyperfine interaction goes with the inverse cube of the distance to the electron and is expected to affect nuclear spin diffusion (as detailed in Introduction). Yet, the dependence of the spin diffusion coefficient with respect to the distance to the electron is not known. The results presented here pave the way toward a detailed study of this dependence.

The quality of the inversion pulses was assessed in a separate experiment presented in the Supplementary Materials (see fig. S6), showing that the inversion has a maximum efficiency over ~3/5 of the theoretical width. Those measurements are used to estimate the polarization of the proton spins at the beginning of detection as a function of their dipolar coupling constant to the electron [see Fig. 8C]. The polarization dip at the center corresponds to the saturated visible spins. Assuming that the offset frequency of the nuclei is governed by the paramagnetic shift, we can translate the offset into a distance (see the Supplementary Materials for the expression of the paramagnetic shift). For a given shift $\Delta\omega$, the distance between the electron and the nucleus can take any value between 0 and r_{e-n}^{max}, depending on the angle between main magnetic field and the vector connecting the electron and the nucleus θ. The maximal possible distance r_{e-n}^{max} corresponds to $\theta = 0, \pi$ and is given by

$$r_{e-n}^{max} = \left(\frac{1}{2}\frac{\mu_0}{4\pi}\frac{\hbar\gamma_e\gamma_n}{|\Delta\omega|}\right)^{1/3} \quad (8)$$

in rad s^{-1}, where μ_0, $\hbar$, γ_e, γ_n, and r are the vacuum permeability, reduced Planck's constant, the gyromagnetic ratios of the electron, and the nucleus and the distance between them, respectively. The profiles in Fig. 8C are expressed as a function of the maximum electron-nucleus distance r_{e-n}^{max} using the above equation and are shown in Fig. 8D.

The nuclei closest to the electron

The HypRes experiment with inversion shows that spins as close as 0.3 nm to the electron can exchange polarization with the visible spins, faster than they relax toward thermal equilibrium. The HypRes experiment with a 4-MHz inversion width causes a stronger negative overshoot than with a 3-MHz inversion width. Therefore, there are spins that are not inverted by the 3-MHz inversion pulse but are inverted by the 4-MHz inversion pulse and yet can still share their polarization with the visible spins. According to Fig. 8D, such spins are at a maximum distance of 0.3 nm to the electron. Ooi Tan *et al.* have shown in 2019 that proton spins within a radius of <0.6 nm to a trityl radical were in contact with the bulk at 100 K and 0.3 T (*37*). Our results confirm this observation at 3.8 K and 7.05 T.

This interpretation relies on the assumption that the inversion pulses are efficient even far away from the center of the NMR line. However, the efficiency of the inversion pulses is diminished at its edges due to the finite width of the resonance of the NMR probe. Furthermore, paramagnetic relaxation in the transverse plane is expected to be intense for far off-resonance nuclei as they are nearer to the electron spin, causing them to relax during the inversion pulse. Yet, because we observe a stronger effect of the inversion as we increase the chirp width, we conclude that the broadest pulse must still be reasonably efficient at its edges. If the 3-MHz inversion pulse was inefficient at its edges, the 4-MHz inversion pulse would not be more efficient over the same range, and the same results would be observed for the two experiments.

It is interesting to remark that a sphere with a radius of 0.3 nm in a solution with 11 M protons contains less than a single proton spin on average. Yet, the TEMPOL molecule itself contains 12 protons on the four methyl groups that surround the radical and a further four protons on the next positions of the ring. As a consequence, the proton spin concentration is stronger in the vicinity of the electron than in the bulk of the sample. This local heterogeneity could be part of the reason why the nuclear polarization appears to escape so easily, a feature that could be used for the rational design of new polarizing agents.

HypRes experiment in MAS-DNP conditions at 100 K

We further apply the HypRes method in the context of MAS-DNP at 100 K on sample II. We chose to use a fully protonated medium to avoid cross-relaxation from deuterium to proton spins and, thus, ensure that any overshoot is strictly due to the contribution of the hidden proton spins (*48*). The high proton concentration results in a strong dipolar broadening of the NMR line, ~70 kHz [see Fig. 9A]. The sample was polarized during 4 s before saturation. Figure 9B shows the microwave-on and -off curves together with the excess. Contrary to the experiments shown in Figs. 6 and 8, each point of the curve was acquired separately using a $\pi/2$ rf pulse and repeating the acquisition with another delay. Although not as strong as at lower temperature, a HypRes overshoot is observed.

Because of the low number of data points at short delays (between 0 and 50 ms), the two-reservoir model cannot be fitted to the data. However, visual inspection of the HypRes curve shows that the maximum of the excess is reached ~30 ms after saturation. The flow rate can thus be estimated to be on the order of $R_f \approx 30\ s^{-1}$. As a comparison, for sample I at 4.2 K in static mode, the maximum of the excess is reached ~3 s after saturation, with a flow rate of $R_f = 0.29\ s^{-1}$, indicating that the flow is two orders of magnitude slower. This may be due to the combined effects of increased spin concentration, MAS, and higher temperature. The low-temperature measurements were performed on sample I, with 11 M protons, while the MAS measurements were performed on sample II, with 110 M. Increasing the proton concentration decreases the average distance

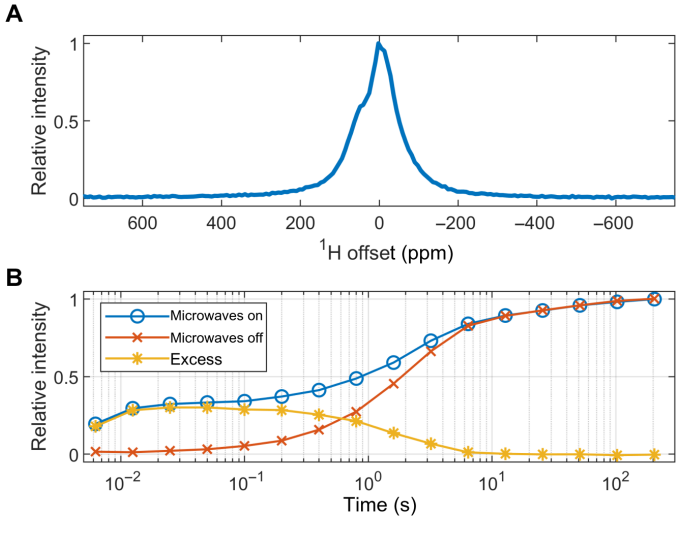

Fig. 9. HypRes under MAS. (**A**) Proton spectrum of sample II at 14.0 T and 100 K under MAS at 8 kHz obtained by DNP. (**B**) Corresponding HypRes curves. Contrary to experiments in static mode at low temperatures, these measurements were obtained with $\pi/2$ pulses, each point being an individual measurement.

between neighbors and, therefore, increases the dipolar couplings and the diffusion coefficient. MAS is known to influence the spin diffusion coefficient and, in some cases, it may enhance spin diffusion (*45*). We note that studying the dependence of the flow rate on the MAS rate would be of great interest but is beyond the scope of the current study.

The CE-DNP mechanism under MAS leads to a depolarized nuclear state with lower polarization compared to Boltzmann equilibrium (*36*, *49*). During the HypRes experiment, after microwaves are turned off, the electrons rapidly return to Boltzmann equilibrium (within $5T_{1,e} \sim 1.5$ ms) (*36*, *49*) and start depolarizing the nuclei. The observation of the overshoot indicates that hidden spins exchange polarization with the visible spins faster than they are depolarized.

The reason why the overshoot is so weak as compared to thermal equilibrium is likely to be explained by the saturation scheme. The visible spins were saturated with a train of 100 pulses separated with 5 ms, which yields a total of 500 ms. As the exchange between the reservoir is on the order of 30 ms, a substantial portion of polarization is able to escape from the hidden reservoir in between pulses resulting in a non-ideal saturation factor of the hidden reservoir η_{sat}. Furthermore, the radical concentration in sample II is five times lower than in sample I, which hides a smaller fraction of the spins and, hence, causes a smaller overshoot.

The favored polarization pathway

Our results show that the flow rate of polarization from hidden to visible spins is highly sensitive to temperature (see Fig. 6). It is as fast as 0.28 s^{-1} at 4.2 K but markedly decreases with temperature reaching a value as low as 4.3×10^{-3} s^{-1} at 1.2 K. This could contribute to the explanation of why DNP becomes slower as temperature decreases. Figure 10A shows DNP build-up curves for sample I between 1.2 and 4.2 K. The proton polarization at DNP equilibrium P_{DNP}^{max} and the build-up rates, $R_{DNP,a}$ and $R_{DNP,b}$, were extracted from the experimental data by fitting a biexponential function

$$P(t) = P_{DNP,max}(1 - a\exp\{-R_{DNP,a}t\} - (1-a)\exp\{-R_{DNP,b}t\}) \quad (9)$$

where a is the weight of the fast rate component $R_{DNP,a}$ and is between 0 and 1. The fit parameters are shown in Fig. 10B. See the Supplementary Materials for more details on the fit and on the choice of the fit function. As the temperature is decreased from 4.2 to 1.2 K, the build-up rate constants drop by more than a factor of 2, from $R_{DNP,a} = 0.037$ s^{-1} and $R_{DNP,b} = 0.018$ s^{-1} to $R_{DNP,a} = 0.018$ s^{-1} and $R_{DNP,b} = 0.004$ s^{-1}.

The fact that diffusion is slower at lower temperature gives a hint as to how the favored polarization pathway is affected by temperature. At 4.2 K, the polarization that builds up in the hidden reservoir can flow out to the visible spins on a time scale, which is fast compared with the DNP build-up time constants. Therefore, the polarization of the hidden reservoir is expected to contribute to the observed signal under DNP. In contrast, at 1.2 K, the flow of polarization from the hidden to visible reservoir that we measured with the HypRes experiment becomes slower than the DNP build-up rates. Therefore, the polarization of the hidden reservoir is not expected to contribute efficiently to the observed signal under DNP.

Possible mechanisms enabling polarization flow

As we pointed out in Introduction, diffusion is expected to be effectively suppressed among the solvent protons of sample I. Yet, our results show that diffusion can occur but strongly depends on temperature. A possible explanation for this breakdown in flow rate at lower temperatures is that nuclear spin diffusion among core nuclei is assisted by electron spin flip-flops. This idea was suggested back in 1971 by Horvitz (*24*–*27*), who showed that the field fluctuations induced by the electronic flip-flops compensate for the energy mismatch between the neighboring core nuclear spins, thus enabling nuclear spin polarization flow. At low temperature, where the polarization of the electron approaches unity, the electron spin flip-flop rate diminishes (*43*), which, in turn, would slow down the polarization flow from hidden to visible nuclear spins. At 1.2 K and 7.05 T, the electron spin polarization exceeds 99.9%, and the electron spin flip-flop probability vanishes, an effect that has been successfully exploited in the past in microwave-gated DNP experiments (*43*). Microwave irradiation diminishes the electron polarization. Experiments in (*43*) were performed in very similar conditions to that of sample I (between 1.2 and 4.2 K) and found that microwave irradiation reduces the electron polarization from ~100 to <40%. The HypRes experiment gives access to the measurement of polarization flow rates in the absence of microwave irradiation. It is hence possible that the flow rate under microwave irradiation, that is, when DNP occurs, is actually higher. Assessing this contribution will be the subject of future work.

One study investigates how phonons can contribute to nuclear spectral spin diffusion, that is, spin diffusion between nuclei whose

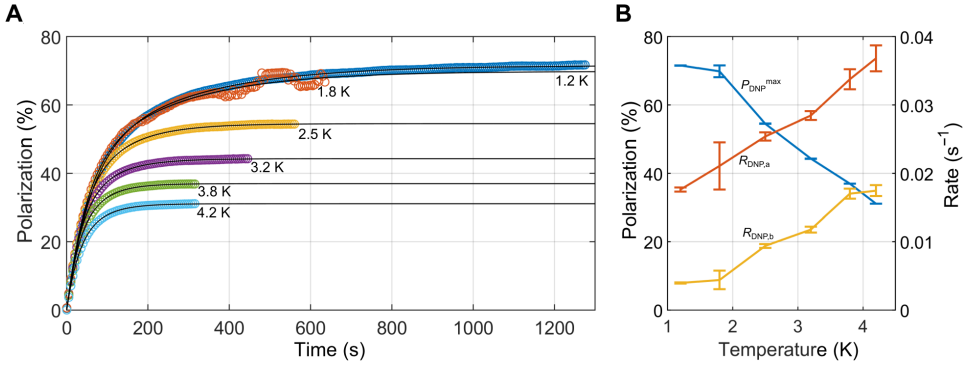

Fig. 10. DNP performance vs. temperature. (**A**) DNP build-up curves for sample I at 7.05 T in static mode between 1.2 and 4.2 K, monitored with small-angle pulses. The colored circles and the black lines represent the experimental data and the biexponential model, respectively. (**B**) Fit parameters of the biexponential model (see Eq. 9), DNP build-up rates $R_{DNP,a}$ and $R_{DNP,b}$, and polarization at the DNP steady state P_{DNP}^{max} plotted against temperature. The error bars correspond to the error of the fit with 95% confidence.

energy is not perfectly matched (*43*). It shows how phonons may introduce temperature dependence into spin diffusion. The authors conclude that "the temperature-dependent spin diffusion […] seems to be a rather general phenomenon, occurring more as a rule than as an exception at temperatures not close to the absolute zero." Such mechanisms could contribute to the temperature dependence of the polarization flow rate measured in our study.

In the context of MAS-DNP, Mentink-Vigier *et al.* (*40*) and Perras *et al.* (*36*, *38*) have both shown that the modulation of the hyperfine interaction by MAS allows polarization transfer from core to bulk proton spins (*34*, *36*). Wittmann *et al.* have reported similar findings on ^{13}C hyperpolarization by endohedral fullerene N@C_{60} as the polarizing agent (*39*). This mechanism could, hence, contribute to the flow of polarization under MAS observed in this study.

The question of the spin diffusion barrier is also raised outside of *d*DNP and MAS-DNP. We note the recent work of Pagliero *et al.* (*50*) in the field of color centers in diamonds used for ^{13}C hyperpolarization. Although they are concerned with a different physical system, they draw conclusions that are similar to ours. They show that nuclear spin diffusion is possible for ^{13}C spins with coupling constants to paramagnetic centers of no less than 100 MHz. Furthermore, they propose a mechanism to account for this peculiar diffusion process.

New perspectives for the study of the diffusion barrier

Over the past two decades, a number of studies have brought insights into diffusion processes in the vicinity of the electron. Modern computational tools enabled quantum mechanical descriptions of multiple-spin systems, replacing continuous models based on diffusion laws. Full quantum mechanical approaches were used to simulate DNP buildups in static conditions (*31*–*33*, *41*, *42*). In these studies, the slowdown of nuclear polarization transfer in the vicinity of the electron is a direct consequence of how the interactions of the system are modeled—the spin barrier does not enter the model as a hypothesis, as in Blumberg or Khustishvili's early works (*17*, *19*). Full quantum mechanical descriptions were also used in a number of studies of MAS-DNP (*30*, *36*, *38*, *40*). In an alternative approach, two studies used rate equations to describe transfer and relaxation within a large number of individual spins, in both static and MAS-DNP (*39*, *51*). One of them used this approach to understand the polarization pathways in static SE-DNP of proton spins at 80 K and 5 T and concluded that polarization transport from the electron directly to bulk nuclei is more efficient than through the intermediate core nuclei (*51*). The other used the same approach to simulate ^{13}C MAS-DNP build-up curves and gave a mechanistic account of how in this context polarization could efficiently be transferred from core to bulk spins (*39*). Last, a recent study used a model based on diffusion laws reminiscent of earlier works but in the context of MAS-DNP (*29*). This approach gave a phenomenological picture of the dependence of polarization transfer in the vicinity of the electron on the concentration of nuclear spins.

The simulations used in these studies—whether based on full quantum mechanical descriptions, rate equations, or temperature-like models—were meant to reproduce DNP build-up curves, which are influenced by the efficiency of both the electron-nucleus polarization transfer (DNP mechanism) and the nucleus-nucleus polarization transfer (spin diffusion). The HypRes experiment allows a study of the second of these contributions separated from the first. Repeating such simulations to model the dynamics of HypRes curves is warranted to bring greater insights into nuclear spin dynamics in the vicinity of the electron.

Conclusion and Outlook

We have shown that the HypRes method allows for the time-resolved monitoring of polarization flow from nuclei in the vicinity of the electron to the visible spins. This process is essential for the efficiency of DNP, which was up to now studied mainly by measuring build-up rates and polarization levels at DNP equilibrium. Our method helps to disentangle the contributions of diffusion from the efficiency of the DNP process itself. The use of broadband inversion pulses further increases the potential of HypRes and permits the observation of diffusion in the nearest environment of the electron among nuclei that cannot be directly detected. The HypRes experiment makes use of microwave gating, which is straightforward to implement in *d*DNP conditions using solid-state microwave sources. We note that the implementation of microwave gating is not as straightforward in the context of MAS-DNP, using gyrotrons. To the best of our knowledge, the capability of performing MAS-DNP experiments with microwave gating within milliseconds is unique to our equipment (*52*).

We applied our method between 1.2 and 4.2 K at 7.05 T in static mode and at 100 K and 14.1 T under MAS. We found that the polarization flow from hidden to visible spins is highly sensitive to temperature and faster than longitudinal relaxation in all studied conditions. We proposed a two-reservoir model to describe the dynamics of the HypRes experiment (without inversion pulses). This approach has the advantage of being simple and able to extract easy-to-interpret parameters from the HypRes curves, namely, the relaxation rate constant of the hidden spins, the flow rate constant between the hidden and visible spins, and the fraction of hidden spins. In the context of DNP at 3.8 K, the HypRes experiment with inversion pulses demonstrated that spins as close as 0.3 nm to the electron can still exchange polarization with the visible spins. We do not find any evidence of a rigid "diffusion barrier" in our conditions, or using Wolfe's terminology, we find that the barrier cannot be larger than 0.3 nm.

Here, we used the HypRes experiment and the two-reservoir model to study the effect of temperature on the flow rate constant. We foresee that this approach can be used to assess the influence of spin diffusion on other experimental parameters, such as dopant concentration and structure, nuclear spin concentration, or the presence of methyl groups, to name only a few. Such insights into spin dynamics could be used to rationally design more elaborate sample architectures that would maximize the polarization transfer from nuclei in the close vicinity of the electron. We also anticipate the use of HypRes as a tool for theoretical studies of spin diffusion. These new measurements can be used to test the validity of models describing the mechanisms allowing for spin diffusion in the vicinity of the electron. We therefore advocate the use of HypRes as a tool to study and potentially improve DNP performance.

MATERIALS AND METHODS

Sample preparation

Sample I

All chemicals were purchased from Sigma-Aldrich. Standard DNP juice with a 50 mM TEMPOL concentration in H_2O:D_2O:glycerol-d_8 (1:3:6, v/v/v) was prepared according to the procedure detailed in

the Supplementary Materials. For each experiment, 100 µl of sample I was placed in a Kel-F sample cup, which is then immersed in the liquid helium bath of our DNP polarizer's cryostat. The rapid insertion of the sample into the cryostat ensures the formation of a glass. To verify that the sample has the expected properties, a ^{1}H DNP build-up curve is recorded at 3.8 K, leading to $P(^1\mathrm{H}) \geq 30\%$ with a build-up time constant $40 \leq \tau_{DNP} \leq 50$ s. In the case of the HypRes experiment with inversion pulses, the batch of sample did not initially form a good glass. To overcome this issue, the sample was frozen by dropping 10 µl of sample in liquid nitrogen. Ten beads were then transferred to the sample cup.

Sample II

The AsymPolPOK was obtained from Sigurdsson's group (*44*), and the glycerol was obtained from Sigma-Aldrich. A 30 mM solution of AsymPolPOK in deionized water was first prepared and then 20 µl was added to a 40-µl solution of glycerol/water (9:1, v/v). This led to a 10 mM AsymPolPOK concentration in glycerol/water (6:4, v/v) solution that was later packed into a 3.2-mm sapphire rotor.

Low-temperature DNP experiments

All low-temperature DNP measurements were performed with a prototype DNP polarizer, "Alpha polarizer," developed by Bruker Biospin based on a helium bath cryostat operating at variable temperatures $1.2 \leq T \leq 4.2$ K and in a magnetic field $B_0 = 7.05$ T. All experiments were performed using microwave frequency irradiation with a Virginia Diode Inc. (VDI) source [8- to 20-GHz synthesizer with a 198-GHz amplifier/multiplier chain (AMC)] VDI 198-GHz AMC) at $f_{\mu w} = 197.569$ GHz with an optimized triangular frequency modulation over $\Delta f_{\mu w} = 160$ at a rate $f_{mod} = 500$ Hz, giving optimum positive proton spin polarization for a standard 50 mM TEMPOL reference sample at 3.8 K when using positive mode DNP. These parameters were used for other temperatures without further optimization. For negative mode DNP, a frequency of $f_{\mu w} = 197.648$ GHz modulated over $f_{mod} = 80$ MHz at 500 Hz was used. The microwave AMC outputs a power $P \approx 125$ mW. Some of the power is lost along the waveguide straight sections, miter bends, and connectors. The microwave power deposited at the sample location was estimated to be $P \approx 30$ mW by comparing the liquid helium evaporation at $T = 1.2$ K under microwave irradiation with that under the effect of a resistive heater placed in the sample space. The helium evaporation was measured using a flow meter (Bronkhorst gas flow meter EL-FLOW Select F-111AC) at the output of the cryostat pump.

The experiments presented in Fig. 8 use chirp pulses that are broadband up to 4 MHz with a sweep rate of 2 MHz/s and a resolution of 10 kpoint/s. To perform these experiments in a satisfactory manner, the Q factor of the probe was diminished by adding a 50-ohm resistance (Barry Industries 50-W BeO flanged resistor) in the NMR circuit.

NMR systems

Dissolution DNP

The NMR probe used to measure proton signals during the 1.2 to 4.2 K DNP experiments is based on locally (in the helium bath) tuned and inductively coupled coils, with remote (outside of the cryostat) tuning and matching with two variable capacitors. All NMR data were acquired at 300.13 MHz with a Bruker Avance III NMR spectrometer operating with TopSpin 3.5.7. Microwave gating was achieved by applying transistor-transistor logic (TTL) pulses on a dedicated port of the VDI AMC that were generated by the Bruker NMR spectrometer with a command directly implemented in the Topspin pulse program (*43*).

Magic angle spinning DNP

All MAS-DNP experiments were performed with a Bruker 600-MHz/395.145-GHz MAS-DNP system, equipped with a 3.2-mm triple-resonance MAS-DNP probe and Bruker Avance III console, controlled by Topspin 3.6.2. The temperatures of the bearing/drive/variable temperature unit were (100/98/92 K) leading to a sample temperature of ~99 K under microwave irradiation and ~93 K without. The microwave setup differs from the standard Bruker MAS-DNP setup as the microwaves are brought and controlled via a quasi-optic system (*52*). This quasi-optic bench is completed with a Martin-Puplett interferometer that improves sample irradiation (*53*). Here, the microwave gating (*52*), controlled through Topspin via TTL pulses, was essential to carry out these experiments.

HypRes experiments

Saturation

The saturation train of pulses used trains of hard pulses between 5 and 15 µs. More details of the saturation procedures are available in the Supplementary Materials.

Monitoring

Because the equilibration of the polarizations of the hidden and visible nuclear spin reservoirs and the observed relaxation can happen on very different time scales, the acquisition blocks are set at variable and optimized delays to better capture the whole polarization resurgence and relaxation trajectory. Alternatively, the detection (steps IV and V, see Fig. 3) can be performed using $\pi/2$ pulses, each point of the curve being acquired in a separated experiment.

Processing

The raw HypRes signal may contain a contribution from the background (coil support and sample holder) and from the signal originating from the return to Boltzmann equilibrium that would be observed if the sample had not been subject to microwave irradiation in the preparation step. These two contributions are suppressed by the following procedure. Each HypRes experiment is repeated twice, without and then with prior microwave irradiation. The microwave-off experiment corresponds to a conventional saturation recovery experiment, acquired with the exact same parameters and delays as the microwave-on experiment (here, we should stress that, even for the microwave-on experiment, the microwaves are only on during the preparation step and not during detection). The microwave-off curve is subtracted from the microwave-on curve to yield a curve expressed as the excess of polarization along time with respect to the thermal equilibrium buildup. In this unit, the horizontal line at 0% polarization corresponds to the saturation recovery line. The processing is illustrated by Fig. 4. Both the microwave-on and -off curves tend toward a polarization of 0.19%, that is, the proton polarization at Boltzmann equilibrium at 3.8 K and 7.05 T. Similarly, the excess of polarization, which is the difference between the two curves, ultimately tends toward 0. All HypRes experiments presented in this study are processed according to this procedure. The y axis on the right of the graph expresses the same quantity in units of thermal equilibrium magnetization. Expressed in this unit, the microwave-on and -off curves tend toward 1.

Data analysis

The data were analyzed using MATLAB R2020b (MathWorks).

SUPPLEMENTARY MATERIALS

Supplementary material for this article is available at http://advances.sciencemag.org/cgi/content/full/7/18/eabf5735/DC1

REFERENCES AND NOTES

1. A. G. M. Rankin, J. Trébosc, F. Pourpoint, J.-P. Amoureux, O. Lafon, Recent developments in MAS DNP-NMR of materials. *Solid State Nucl. Magn. Reson.* **101**, 116–143 (2019).
2. Ü. Akbey, H. Oschkinat, Structural biology applications of solid state MAS DNP NMR. *J. Magn. Reson.* **269**, 213–224 (2016).
3. Z. J. Wang, M. A. Ohliger, P. E. Z. Larson, J. W. Gordon, R. A. Bok, J. Slater, J. E. Villanueva-Meyer, C. P. Hess, J. Kurhanewicz, D. B. Vigneron, Hyperpolarized ^{13}C MRI: State of the art and future directions. *Radiology* **291**, 273–284 (2019).
4. D. A. Hall, D. C. Maus, G. J. Gerfen, S. J. Inati, L. R. Becerra, F. W. Dahlquist, R. Griffin, Polarization-enhanced NMR spectroscopy of biomolecules in frozen solution. *Science* **276**, 930–932 (1997).
5. J. H. Ardenkjær-Larsen, B. Fridlund, A. Gram, G. Hansson, L. Hansson, M. H. Lerche, R. Servin, M. Thaning, K. Golman, Increase in signal-to-noise ratio of > 10,000 times in liquid-state NMR. *Proc. Natl. Acad. Sci. U.S.A.* **100**, 10158–10163 (2003).
6. J. H. Ardenkjaer-Larsen, On the present and future of dissolution-DNP. *J. Magn. Reson.* **264**, 3–12 (2016).
7. F. Jähnig, G. Kwiatkowski, M. Ernst, Conceptual and instrumental progress in dissolution DNP. *J. Magn. Reson.* **264**, 22–29 (2016).
8. B. Plainchont, P. Berruyer, J.-N. Dumez, S. Jannin, P. Giraudeau, Dynamic nuclear polarization opens new perspectives for NMR spectroscopy in analytical chemistry. *Anal. Chem.* **90**, 3639–3650 (2018).
9. S. Jannin, J.-N. Dumez, P. Giraudeau, D. Kurzbach, Application and methodology of dissolution dynamic nuclear polarization in physical, chemical and biological contexts. *J. Magn. Reson.* **305**, 41–50 (2019).
10. M. Rosay, M. Blank, F. Engelke, Instrumentation for solid-state dynamic nuclear polarization with magic angle spinning NMR. *J. Magn. Reson.* **264**, 88–98 (2016).
11. M. Baudin, B. Vuichoud, A. Bornet, G. Bodenhausen, S. Jannin, A cryogen-consumption-free system for dynamic nuclear polarization at 9.4 T. *J. Magn. Reson.* **294**, 115–121 (2018).
12. J. H. Ardenkjær-Larsen, S. Bowen, J. R. Petersen, O. Rybalko, M. S. Vinding, M. Ullisch, N. C. Nielsen, Cryogen-free dissolution dynamic nuclear polarization polarizer operating at 3.35 T, 6.70 T, and 10.1 T. *Magn. Reson. Med.* **81**, 2184–2194 (2019).
13. K. Kundu, F. Mentink-Vigier, A. Feintuch, S. Vega, DNP mechanisms. *eMagRes.* **8**, 295–338 (2019).
14. A. Abragam, M. Goldman, Principles of dynamic nuclear polarisation. *Rep. Prog. Phys.* **41**, 395–467 (1978).
15. W. T. Wenckebach, Dynamic nuclear polarization via the cross effect and thermal mixing: A. The role of triple spin flips. *J. Magn. Reson.* **299**, 124–134 (2019).
16. N. Bloembergen, On the interaction of nuclear spins in a crystalline lattice. *Physica* **15**, 386–426 (1949).
17. W. E. Blumberg, Nuclear spin-lattice relaxation caused by paramagnetic impurities. *Phys. Rev.* **119**, 79–84 (1960).
18. G. R. Khutsishvili, Spin diffusion and magnetic relaxation of nuclei. *Sov. Phys. J. Exp. Theor. Phys.* **15**, 909–913 (1962).
19. G. R. Khutsishvili, Spin diffusion, magnetic relaxation and dynamic polarization of nuclei. *Sov. Phys. J. Exp. Theor. Phys.* **16**, 1540–1543 (1963).
20. I. J. Lowe, D. Tse, Nuclear spin-lattice relaxation via paramagnetic centers. *Phys. Rev.* **166**, 279–291 (1968).
21. M. Goldman, Impurity-controlled nuclear relaxation. *Phys. Rev.* **138**, A1675–A1681 (1965).
22. T. J. Schmugge, C. D. Jeffries, High dynamic polarization of protons. *Phys. Rev.* **138**, 1785–1801 (1965).
23. H. E. Rorschach Jr., Nuclear relaxation in solids by diffusion to paramagnetic impurities. *Physica* **30**, 38–48 (1964).
24. E. P. Horvitz, Nuclear spin diffusion induced by paramagnetic impurities in nonconducting solids. *Phys. Rev. B.* **3**, 2868–2872 (1971).
25. L. L. Buishvili, M. D. Zviadadze, B. D. Mikaberidze, Nuclear cross-relaxation induced by a paramagnetic impurity. *Sov. Phys. J. Exp. Theor. Phys.* **69**, 1077–1079 (1975).
26. K. K. Sabirov, Nuclear flip-flop transitions induced by paramagnetic impurities. *Phys. Status Solidi.* **91**, 735–739 (1979).
27. V. V. Demidov, V. A. Atsarkin, Nuclear magnetic relaxation and spin diffusion in the local fields of paramagnetic centers. *Sov. Phys. J. Exp. Theor. Phys.* **79**, 726–732 (1980).
28. J. P. Wolfe, Direct observation of a nuclear spin diffusion barrier. *Phys. Rev. Lett.* **31**, 907–910 (1973).
29. N. A. Prisco, A. C. Pinon, L. Emsley, B. F. Chmelka, Scaling analyses for hyperpolarization transfer across a spin-diffusion barrier and into bulk solid media. *Phys. Chem. Chem. Phys.* **23**, 1006–1020 (2021).
30. F. A. Perras, M. Raju, S. L. Carnahan, D. Akbarian, A. C. T. van Duin, A. J. Rossini, M. Pruski, Full-scale ab initio simulation of magic-angle-spinning dynamic nuclear polarization. *J. Phys. Chem. Lett.* **11**, 5655–5660 (2020).
31. A. Karabanov, G. Kwiatkowski, W. Köckenberger, Spin dynamic simulations of solid effect DNP: The role of the relaxation superoperator. *Mol. Phys.* **112**, 1838–1854 (2014).
32. Y. Hovav, A. Feintuch, S. Vega, Dynamic nuclear polarization assisted spin diffusion for the solid effect case. *J. Chem. Phys.* **134**, 074509 (2011).
33. Y. Hovav, A. Feintuch, S. Vega, Theoretical aspects of dynamic nuclear polarization in the solid state—The solid effect. *J. Magn. Reson.* **207**, 176–189 (2010).
34. C. Ramanathan, Dynamic nuclear polarization and spin diffusion in nonconducting solids. *Appl. Magn. Reson.* **34**, 409–421 (2008).
35. S. K. Jain, C.-J. Yu, C. B. Wilson, T. Tabassum, D. E. Freedman, S. Han, Dynamic nuclear polarization with vanadium(IV) metal centers. *Chem* **7**, 421–435 (2021).
36. F. A. Perras, M. Pruski, Linear-scaling ab initio simulations of spin diffusion in rotating solids. *J. Chem. Phys.* **151**, 034110 (2019).
37. K. Ooi Tan, M. Mardini, C. Yang, J. H. Ardenkjaer-Larsen, R. G. Griffin, Three-spin solid effect and the spin diffusion barrier in amorphous solids. *Sci. Adv.* **5**, eaax2743 (2019).
38. F. A. Perras, M. Pruski, Large-scale ab initio simulations of MAS DNP enhancements using a Monte Carlo optimization strategy. *J. Chem. Phys.* **149**, 154202 (2018).
39. J. J. Wittmann, M. Eckardt, W. Harneit, B. Corzilius, Electron-driven spin diffusion supports crossing the diffusion barrier in MAS DNP. *Phys. Chem. Chem. Phys.* **20**, 11418–11429 (2018).
40. F. Mentink-Vigier, S. Vega, G. De Paëpe, Fast and accurate MAS-DNP simulations of large spin ensembles. *Phys. Chem. Chem. Phys.* **19**, 3506–3522 (2017).
41. D. Wiśniewski, A. Karabanov, I. Lesanovsky, W. Köckenberger, Solid effect DNP polarization dynamics in a system of many spins. *J. Magn. Reson.* **264**, 30–38 (2016).
42. A. Karabanov, D. Wiśniewski, I. Lesanovsky, W. Köckenberger, Dynamic nuclear polarization as kinetically constrained diffusion. *Phys. Rev. Lett.* **115**, 020404 (2015).
43. J. Dolinšek, P. M. Cereghetti, R. Kind, Phonon-assisted spin diffusion in solids. *J. Magn. Reson.* **146**, 335–344 (2000).
44. F. Mentink-Vigier, I. Marin-Montesinos, A. P. Jagtap, T. Halbritter, J. Van Tol, S. Hediger, D. Lee, S. T. Sigurdsson, G. De Paëpe, Computationally assisted design of polarizing agents for dynamic nuclear polarization enhanced NMR: The asympol family. *J. Am. Chem. Soc.* **140**, 11013–11019 (2018).
45. M. Roos, P. Micke, K. Saalwächter, G. Hempel, Moderate MAS enhances local ^{1}H spin exchange and spin diffusion. *J. Magn. Reson.* **260**, 28–37 (2015).
46. C. P. Jaroniec, Solid-state nuclear magnetic resonance structural studies of proteins using paramagnetic probes. *Solid State Nucl. Magn. Reson.* **43–44**, 1–13 (2012).
47. A. J. Pell, G. Pintacuda, C. P. Grey, Paramagnetic NMR in solution and the solid state. *Prog. Nucl. Magn. Reson. Spectrosc.* **111**, 1–271 (2019).
48. M. M. Hoffmann, S. Bothe, T. Gutmann, F.-F. Hartmann, M. Reggelin, G. Buntkowsky, Directly vs indirectly enhanced ^{13}C in dynamic nuclear polarization magic angle spinning NMR experiments of nonionic surfactant systems. *J. Phys. Chem. C* **121**, 2418–2427 (2017).
49. F. Mentink-Vigier, S. Paul, D. Lee, A. Feintuch, S. Hediger, S. Vega, G. De Paëpe, Nuclear depolarization and absolute sensitivity in magic-angle spinning cross effect dynamic nuclear polarization. *Phys. Chem. Chem. Phys.* **17**, 21824–21836 (2015).
50. D. Pagliero, P. R. Zangara, J. Henshaw, A. Ajoy, R. H. Acosta, J. A. Reimer, A. Pines, C. A. Meriles, Optically pumped spin polarization as a probe of many-body thermalization. *Sci. Adv.* **6**, eaaz6986 (2020).
51. A. A. Smith, B. Corzilius, A. B. Barnes, T. Maly, R. G. Griffin, Solid effect dynamic nuclear polarization and polarization pathways. *J. Chem. Phys.* **136**, 015101 (2012).
52. T. Dubroca, A. N. Smith, K. J. Pike, S. Froud, R. Wylde, B. Trociewitz, J. McKay, F. Mentink-Vigier, J. van Tol, S. Wi, W. Brey, J. R. Long, L. Frydman, S. Hill, A quasi-optical and corrugated waveguide microwave transmission system for simultaneous dynamic nuclear polarization NMR on two separate 14.1 T spectrometers. *J. Magn. Reson.* **289**, 35–44 (2018).
53. K. R. Thurber, A. Potapov, W.-M. Yau, R. Tycko, Solid state nuclear magnetic resonance with magic-angle spinning and dynamic nuclear polarization below 25 K. *J. Magn. Reson.* **226**, 100–106 (2013).
54. G. R. Khutsishvili, Spin diffusion. *Sov. Phys. Uspekhi.* **8**, 743–769 (1966).

Acknowledgments: We acknowledge Bruker Biospin for providing the prototype *d*DNP polarizer and particularly D. Eshchenko, R. Melzi, M. Rossire, M. Sacher, and J. Kempf for scientific and technical support. We additionally acknowledge A. Trabesinger for advice on the writing of the manuscript, B. Chmelka and J.-N. Dumez for discussions, C. Jose and C. Pages for use of the ISA Prototype Service, and S. Martinez of the UCBL mechanical workshop for machining parts of the experimental apparatus. **Funding:** This research was supported by ENS-Lyon, the French CNRS, Lyon 1 University, the European Research Council under the European Union's Horizon 2020 research and innovation program (ERC grant agreement no. 714519/HP4all and Marie Skłodowska-Curie grant agreement no. 766402/ZULF). The NHMFL is supported by NSF/DMR 1644779 and the State of Florida,

NIH S10 OD018519, NIH P41 GM122698 01, and NSF CHE 1229170. **Author contributions:** Q.S. and S.J. conceived the experiment. Q.S., S.F.C., F.M.-V., and O.C. carried out the experiments. Q.S. analyzed the data. S.J.E. assisted Q.S. in constructing the model. Q.S. and S.J. wrote the paper. A.C.P. assisted in interpreting the data. **Competing interests:** The authors declare that they have no competing interests. **Data and materials availability:** All data needed to evaluate the conclusions in the paper are present in the paper and/or the Supplementary Materials. All raw data used are available at doi:10.5061/dryad.fttdz08s3.

Submitted 10 November 2020
Accepted 11 March 2021
Published 30 April 2021
10.1126/sciadv.abf5735

Citation: Q. Stern, S. F. Cousin, F. Mentink-Viger, A. C. Pinon, S. J. Elliott, O. Cala, S. Jannin, Direct observation of hyperpolarization breaking through the spin diffusion barrier. *Sci. Adv.* **7**, eabf5735 (2021).

Science Advances

Direct observation of hyperpolarization breaking through the spin diffusion barrier

Quentin Stern, Samuel François Cousin, Frédéric Mentink-Vigier, Arthur César Pinon, Stuart James Elliott, Olivier Cala and Sami Jannin

Sci Adv **7** (18), eabf5735.
DOI: 10.1126/sciadv.abf5735

Science Advances (ISSN 2375-2548) is published by the American Association for the Advancement of Science, 1200 New York Avenue NW, Washington, DC 20005. The title *Science Advances* is a registered trademark of AAAS.